A peridynamic model for oxidation and damage in zirconium carbide ceramics

Francesco Scabbia [a,*], Claudia Gasparrini [b], Mirco Zaccariotto [a,c], Ugo Galvanetto [a,c], Florin Bobaru [d]

[a] *Center of Studies and Activities for Space (CISAS) - "G. Colombo", via Venezia 15, Padova, 35131, Italy*
[b] *Department of Materials and Centre for Nuclear Engineering, Imperial College London, Exhibition Road, London SW 7 2AZ, United Kingdom*
[c] *Department of Industrial Engineering, University of Padova, via Venezia 1, Padova, 35131, Italy*
[d] *Department of Mechanical and Materials Engineering, University of Nebraska-Lincoln, Lincoln, NE, 68588-0526, USA*

ARTICLE INFO

ABSTRACT

Zirconium carbide (ZrC) has potential to be applied in next-generation nuclear reactors for space missions and industrial applications. The mechanisms controlling ZrC oxidation dependence on temperature, material composition, pressure, porosity are not fully understood. In this work, we use a peridynamic modeling of diffusion/reaction across several regions observed in previous experiments to explain the oxygen diffusion mechanism and reaction kinetics. We emphasize the importance in the oxidation and damage process of a transition layer of partially-oxidized ZrC. The peridynamic model has an autonomously moving oxidation interface, and the delamination/detachment of oxide (induced by large volumetric expansion) is simulated here with an oxygen concentration-driven damage model. Once the diffusion properties are calibrated to match the measured oxygen concentration across the oxidation front, the speed of propagation of the oxidation front is predicted by a 1D peridynamic model in excellent agreement with experimental observations. An extension to 2D finds the shape of remaining unoxidized ZrC conforming to experimental observations.

1. Introduction

Nowadays nuclear power plays a fundamental role in reducing the environmental impact of energy and electricity production, thanks to its low CO_2 emissions. Future applications beyond electricity production are also regaining interest. Nuclear thermal propulsion (NTP) reactor, for space applications, is being reconsidered because of the high energy density and superior engine efficiency compared to conventional space propulsion systems. The use of an NTP system enables to halve the duration of space missions, reducing the exposure of astronauts to harmful radiations and other hazards found in space. At the same time, the deployment of Very-High-Temperature Reactors (VHTR) [1] or High-Temperature Gas Reactors (HTGR) [2] will offer increased outlet temperature fluids that can serve industrial processes like high-temperature electrolysis and thermolysis. One of the major challenges for these innovative and advanced nuclear applications rely on the development of materials that can withstand the harsh conditions present during operation in these reactors.

To improve the knowledge about the performance of these advanced materials, the use of both experimental and modeling efforts is essential. In this regard, this work focuses the attention on the understanding and modeling of the oxidation behavior of zirconium carbide (ZrC). ZrC has attractive properties such as high melting point (~3500 K), high thermal conductivity at very high temperatures and low neutron absorption cross section, and is a candidate material for the development of NTP systems for space and a substitute material for SiC in the tri-isotropic coated nuclear fuel (TRISO) particles thanks to its promising fission products retention [3]. One of the drawbacks of ZrC is its affinity to oxygen, since ZrC is often considered an oxygen getter, and poor oxidation resistance.

The oxidation of ZrC proceeds readily and with a considerable associated volume increase which changes materials dimensions [4]. The oxidation mechanism is affected by several parameters such as temperature, partial pressure of oxygen and materials chemical composition. The oxide layer can assume different crystal lattice structures depending on the environmental temperature, oxygen partial pressure and oxygen content. Thermo-mechanical properties and oxidation resistance properties for ZrC are heavily debated in the literature due to

its high degree of non-stoichiometric range [5,6]. Moreover, the transition between unoxidized and oxidized material involves a volumetric expansion that induces stresses in the oxide layer. Analyses of internal stresses induced by oxidation/corrosion processes that involve volumetric expansion are reported, for example, in [7,8]. Crack initiation and propagation within the oxide layer accelerate the oxygen penetration because they generate preferential paths towards the bulk of the body causing significant volume expansion and stresses which need to be better understood and predicted, especially when ZrC is found in a sandwich structure in coatings.

Several experiments have been carried out on the oxidation of carbides or nitrides of this class of materials often named Ultra-High Temperature Ceramics (UHTCs) [4,9–11]. Furthermore, some numerical models have been developed based on classical continuum mechanics and making use of the Finite Element Method (FEM): in [12] the stress distribution arising from the tetragonal-to-monoclinic phase transformation of a single grain of zirconium oxide is computed and in [13] an oxidation model is proposed based on the assumption of the a priori knowledge of the interface motion. Neither of these models was designed to or is capable of predicting the autonomous motion of the carbide-oxide interface, like it has been developed in this work.

Peridynamics is a nonlocal continuum theory which allows for discontinuities in the displacement field to initiate and evolve spontaneously [14,15]. This theory has already been extended to diffusion phenomena [16,17] and multi-physics problems involving diffusion with a moving interface [18–20]. Oxidation phenomena have been dealt with by means of peridynamic modeling in [21,22]. The peridynamic modeling of fracture in a single grain of zirconia undergoing a transformation (involving volume expansion) from tetragonal to monoclinic phase, can be found in [23]. In [24], a peridynamic thermomechanical model to simulate crack propagation in a TRISO particle is presented. However, to the best of our knowledge, no numerical model able to capture the motion of the oxidation interface without a priori assumptions has been developed yet.

The aim of this work is to develop a numerical tool, based on the peridynamic framework, able to predict the evolution, in time, of the carbide-oxide interface. To do so, we use the experimental data described in [4] as reference to compare the numerical results of the proposed model. This experiment consists in exposing a cubic sample of hot-pressed zirconium carbide, maintained at a constant temperature (1073 K), to an oxidative environment. The transition of the cubic sample to a Maltese-cross shape and the formation of cracks leading to the repeated delamination/detachment of the oxide from the carbide bulk can be observed in Fig. 1 (experimental results published in [4]). These experiments in [4] enabled to assess the oxygen concentration profile across different layers formed during oxidation of ZrC. The different layers are comprised by the ZrC bulk, an intermediate dense layer made primarily of carbon and tetragonal zirconium oxide (t-ZrO$_2$) and an outer cracked layer made of monoclinic zirconia (m-ZrO$_2$). These experimental results, obtained in [4], are used to calibrate the peridynamic model parameters to the diffusion/reaction properties of the materials. Once the calibration to material properties is implemented, the proposed peridynamic model is able to capture the evolution in time of the oxygen concentration profile and to predict the propagation speed of the oxidation front in excellent agreement with the experimental observations.

The proposed model is extended to a range of temperatures up to 1173 K with a recalibration of the material properties. Above 1273 K, the oxidation mechanism appears to change as the intermediate layer is no longer present [4], so a modification to the peridynamic model might be required for extending its validity for higher temperatures. This model can also be used to describe the oxidation of transition metal carbides of group IV by accordingly recalibrating the material properties. A limitation in the applicability of the model is given by the availability of the material properties. Those properties can be obtained

with experimental measures, with a calibration process, or potentially with atomistic first-principles calculations.

A similar approach to the one introduced here may be used in modeling damage in lithium-ion batteries, due to the similarities between the type of oxidation phenomenon discussed here and lithiation. Electrodes in solid-state batteries may experience fracture (with a subsequent reduction of life cycles) due to lithium diffusion and intercalation that causes volumetric expansion of the storage material [25,26]. Many experiments and numerical models on this phenomenon have been developed in the literature [27–36]. A peridynamic model of lithiation based on the same principles used in this paper may enhance the understanding of the phenomenon and, possibly, increase the life time of lithium-ion batteries.

The paper is structured as follows. Section 2 summarizes the experimental setup, methodology and results described in [4] for the oxidation of the zirconium carbide. Section 3 gives a brief review of the peridynamic theory applied to diffusion problems and its discretized equations. Section 4 presents the numerical approach to model the zirconium carbide oxidation. Section 5 shows the calibration process of the diffusivity values based on the experimental observations, the variation of the numerical results at different temperatures, and the qualitative validation of the model in a 2D scenario. Section 6 presents conclusions and suggests potential areas for future investigation.

2. Brief review of experimental results

In [4], a hot pressed sintered ZrC sample was oxidized inside a furnace and exposed to ^{16}O oxygen atmosphere for 4 min and to ^{18}O oxygen atmosphere for 4 more minutes, approximately at a temperature of 1073K. A Secondary Ion Mass Spectroscopy (SIMS) analysis has been carried out to obtain the oxygen concentration across the oxidation front. The total oxygen concentration across the sample cross-section is monitored in the numerical simulations, so the sum of the measured concentrations of the two isotopes is considered here. Details of the experiments can be found in [4]. The oxygen concentration has been normalized by dividing it by the highest concentration value of the experimental data and replotted in Fig. 2. Three different regions can be clearly distinguished across the cross-section:

- The outer layer of cracked zirconium oxide where the normalized oxygen concentration is close to 1 (red region);
- The *intermediate layer*, which is a layer of undamaged oxide, where the concentration is close to 0.5 (light blue region);
- The zirconium carbide where the concentration is close to 0 (blue region at the bottom of the image).

The other regions with a very low concentration within the oxide and the intermediate layer are due to the presence of pores, since this experimental analysis is able to detect the oxygen content only in the solid matter.

The zirconium oxide is known to exhibit polymorphs that are stable in different temperature ranges. From the chemical analyses carried out in [4], the cracked zirconium oxide is the monoclinic phase, which is stable at 1073 K. We will denote this phase by m-ZrO$_2$. On the other hand, the zirconium oxide in the intermediate layer exhibits the presence of carbon and the tetragonal oxide phase, which is thermodynamically unstable at 1073 K. In fact, since the tetragonal zirconia is found approximately above 1473 K, this is not the expected polymorph at those experimental conditions. The presence of tetragonal ZrO$_2$ can be related to either stresses in the system or oxygen vacancies. The tetragonal zirconia will be denoted by t-ZrO$_2$. Furthermore, we will denote the zirconium carbide by ZrC.

In [4], the oxygen diffusion coefficient was measured thanks to the use of a ^{18}O tracer by observing the diffusion profile across the intermediate layer. The value for the oxygen diffusion coefficient ($D = 0.09\ \mu m^2/s$) was determined by fitting the experimental results with the analytical solution derived from Fick's second law for a semi-infinite
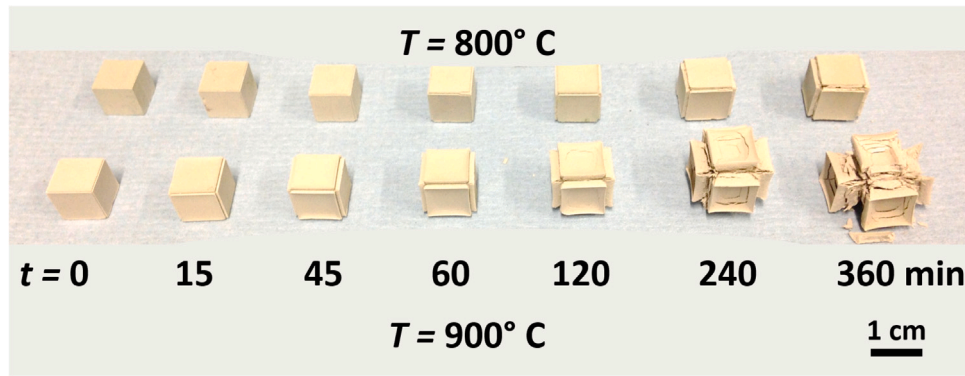
Fig. 1. Photograph of a cubic ZrC sample during the oxidation phenomenon with different environmental temperatures [4]. The mechanical properties of the zirconium carbide are clearly compromised.
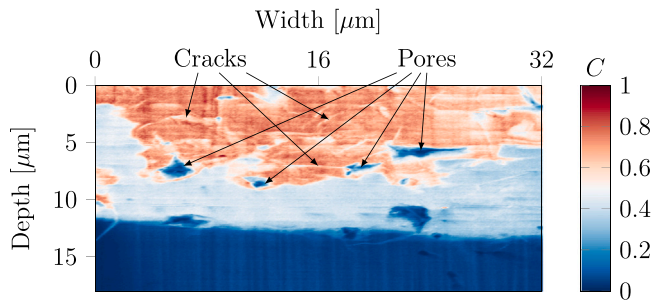

Fig. 2. Normalized oxygen concentration (sum of both ^{16}O and ^{18}O isotopes) obtained with the Secondary Ion Mass Spectroscopy (SIMS) analysis obtained in [4] for a ZrC sample oxidized at 1073 K. The vertical axis represents the depth inside the material, where the external surface lies at 0 μm. For the original experimental data and details on the SIMS analysis, please see [4].
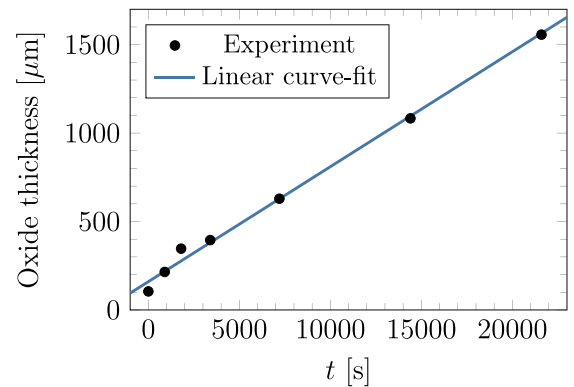

Fig. 3. Oxide growth in time at 1073 K, its linear curve-fit [4] represents only the steady portion of the growth.

medium with a constant source of oxygen. However, it is important to note that this approach relied on certain simplifying assumptions that impact the calibration of the diffusivity. In fact, the approach used in [4] for diffusivity calibration considered solely the concentration profile of the intermediate layer. As we shall see, a transition layer is also present at the interface between the intermediate layer and the ZrC bulk. Furthermore, the approach in [4] assumes that the boundary, i.e., the interface between the cracked (m-ZrO$_2$) and undamaged (t-ZrO$_2$) phases of the oxide, remains stationary. However, it is important to acknowledge that the reaction occurs during oxidation with the ^{18}O isotope, leading to movement of that interface within the considered time frame. In order to address these limitations, we present in Section 4 a peridynamic model predicting the mechanism of ZrC oxidation, in which the diffusion/reaction properties of the materials are calibrated directly from the experimental data.

Oxide growth is of paramount importance in many applications. The oxide thickness of a cubic ZrC sample exposed to an oxidizing environment has been measured at different stages of the oxidation [4]. Since the oxidized samples present a peculiar shape of a Maltese cross, the oxide layer measurements were made through sample cross-section made at the center of the faces to avoid the corners where the oxide thickness grows faster. These experiments showed that the oxide grows linearly in time, as shown in Fig. 3.

The linear growth is in agreement with the observations made on the oxide cross section showing a porous, cracked, non-protective oxide layer: the stable phase of the oxide cracks and tends to delaminate/detach allowing oxygen to access easier pathways of ingression. This mechanism generates an intermediate layer with a constant thickness moving at a constant rate. Furthermore, the growth rate of the oxide thickness depends on temperature. At the temperature of 1073K,

the rate constant, obtained by the slope of the linear fitting shown in Fig. 3, is equal to 0.065 μm/s [4].

Remark 1. Note that $t = 0$ s in Fig. 3 is the time at which the temperature reaches the value of 1073 K, value which is then kept constant. As the temperature rises, some oxidation takes place, which is why the first experimental point does not coincide with the origin. At time $t = 0$ s the temperature is constant, but there is still a transient phenomenon that is not captured by the linear curve fit. Since the model proposed in Section 4 considers only the steady-state (isothermal) condition, the oxide thickness at $t = 0$ s is equal to 0 μm in the simulations. Therefore, when a visual comparison is required between the numerical results and the experimental data, one of the two plots needs to be translated due to this initial offset between experimental and numerical results. In other words, the steady state is fully described just by the slope of the linear curve-fit.

3. Peridynamic modeling of diffusion

Points within a body $\mathcal{B}$ modeled with peridynamics interact with each other through *bonds* [14,15]. The maximum length of a bond between any two points is limited to a finite value denoted as δ and referred to as the *horizon size*, as shown in Fig. 4. In the peridynamic model of ZrC oxidation, the horizon size represents the thickness of the transition layer between pure zirconium carbide and the undamaged phase of the oxide. The calibration of the horizon size to this physical parameter is presented in Section 4.4. Bond properties are calibrated against classical (measured) properties and are named after them by adding the prefix "micro-".
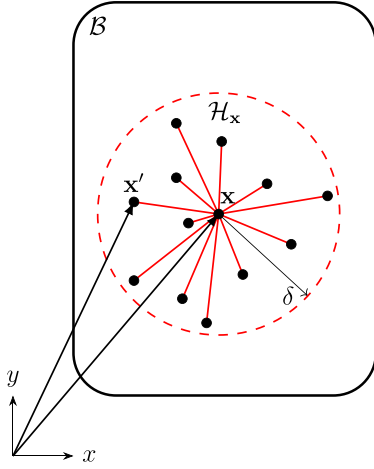
Fig. 4. Neighborhood $\mathcal{H}_{\mathbf{x}}$ of a point in a peridynamic body $\mathcal{B}$: red lines represent the interactions (bonds) between points. (For interpretation of the references to color in this figure legend, the reader is referred to the web version of this article.)

We use an effective diffusion-controlled model to simulate the evolution of oxidation because of the similarities of the phenomenon with the corrosion damage models [18,19,37–43]. In those models, the micro-dissolvability of bonds with one end in the metal and the other in the electrolyte are calibrated to the corrosion rate, whereas the micro-diffusivity of bonds with both ends in the electrolyte are calibrated to the diffusivity of dissolved metal ions in the electrolyte. Similarly, in the ZrC oxidation model, the micro-oxidability of bonds with one end in the carbide phase and the other in the oxide phase are calibrated to the oxidation rate, whereas the micro-diffusivity of bonds with both ends in the oxide phase are calibrated to the diffusivity of oxygen in the oxide phase.

In a peridynamic body, a point $\mathbf{x}$ interacts with a set of points defined as $\mathcal{H}_{\mathbf{x}} = \{\mathbf{x}' \in \mathcal{B} : |\mathbf{x}' - \mathbf{x}| \le \delta\}$, which is known as the *neighborhood* of point $\mathbf{x}$. The neighborhood is respectively a segment, a disk or a sphere in 1D, 2D or 3D bodies. The horizon size can be thought of as a material length-scale, or as a surrogate for a combination of multiple length-scales, if they are present. When comparing against classical models, which usually lack length-scales, one, however, takes the horizon size to go to zero. This is called δ-convergence, see [44].

The peridynamic equation governing diffusion phenomena is given as [18,19]

$$\frac{\partial C(\mathbf{x},t)}{\partial t} = \int_{\mathcal{H}_{\mathbf{x}}} k(\mathbf{x},\mathbf{x}',t) \frac{C(\mathbf{x}',t) - C(\mathbf{x},t)}{\|\mathbf{x}' - \mathbf{x}\|^2} \mathrm{d}V_{\mathbf{x}'}$$
$$= \int_{\mathcal{H}_{\mathbf{x}}} \mathrm{j}(\mathbf{x},\mathbf{x}',t) \mathrm{d}V_{\mathbf{x}'}, \tag{1}$$

where C is the concentration of oxygen, k is the micro-diffusivity (or micro-oxidability, see Remark 2), $V_{\mathbf{x}'}$ is the volume of point $\mathbf{x}'$, d is the micro-diffusivity, and $\mathrm{j}(\mathbf{x},\mathbf{x}',t)$ is the micro-flux. In this work we adopted the kernel function constructed in [45] with the bond length in the denominator appearing with the $n = 2$ exponent. The 2D and 1D governing equations can be obtained by considering respectively a unit thickness h, such that $\mathrm{d}V_{\mathbf{x}'} = h\mathrm{d}A_{\mathbf{x}'} = \mathrm{d}A_{\mathbf{x}'}$, and a unit area A, such that $\mathrm{d}V_{\mathbf{x}'} = A\mathrm{d}x' = \mathrm{d}x'$. The micro-diffusivity k is calibrated to the measured diffusivity (or oxidation rate) K as follows [16–18]:

$$k(\mathbf{x},\mathbf{x}',t) = \begin{cases} \dfrac{K}{\delta} & \text{in 1D,} \\ \dfrac{4K}{\pi\delta^2} & \text{in 2D,} \\ \dfrac{9K}{2\pi\delta^3} & \text{in 3D.} \end{cases} \tag{2}$$

Therefore, the micro-diffusivity has different units for different number of dimensions of the model: [m/s] in 1D, [1/s] in 2D, and [1/(m s)] in 3D.
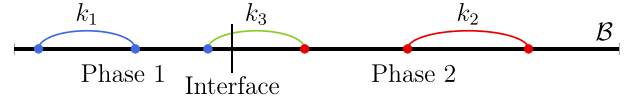

Fig. 5. Three possible types of bonds for diffusion in a 1D body of a two-phase material.

Remark 2. Similarly to the peridynamic corrosion model [39], the bond property k can represent different physical mechanisms depending on the phase of the points that the bond itself connects. In the ZrC oxidation, if a bond connects two points in the oxide phase, k is called "micro-diffusivity" d and represents the diffusion of oxygen. If a bond connects a point in the oxide phase and a point in the carbide phase, k is called "micro-oxidability" r and represents the oxidation of the carbide modeled as a diffusion-controlled reaction. These aspects are discussed in detail in Section 4.2.

When the peridynamic diffusion model is used to describe a two-phase material with a moving interface, the phase of each point may change depending on its current concentration [18]. If $\widehat{C}$ denotes the concentration of phase change, the micro-diffusivity of a bond is determined as [18]:

$$k(x,x',t) = \begin{cases} k_1 & \text{if } C(\mathbf{x},t) < \widehat{C} \text{ and } C(\mathbf{x}',t) < \widehat{C}, \\ k_2 & \text{if } C(\mathbf{x},t) > \widehat{C} \text{ and } C(\mathbf{x}',t) > \widehat{C}, \\ k_3 & \text{if } C(\mathbf{x},t) \le \widehat{C} \le C(\mathbf{x}',t) \text{ or } C(\mathbf{x}',t) \le \widehat{C} \le C(\mathbf{x},t), \end{cases} \tag{3}$$

where k_1, k_2, and k_3 may have different values. Fig. 5 shows the three possible types of bonds when phase 1 is characterized by a concentration smaller than $\widehat{C}$ and phase 2 by a concentration higher than $\widehat{C}$. Therefore, in a peridynamic diffusion model, the interface moves autonomously depending on $\widehat{C}$ and the microdiffusivities k_1, k_2, and k_3. Note that this model does not require any special conditions at the interface, such as Stefan condition (that is instead required in classical models [46–48]). Hence, any results obtained with a peridynamic diffusion model, such as the constant velocity of the interface in Fig. 15, are not prescribed a priori, but are a *prediction* provided by the model [18].

3.1. Discretization of the peridynamic equations

The discretization of the peridynamic diffusion equation can be carried out by means of several different methods, such as the mesh-free method [49–51], the Finite Element Method [52,53] or the Fast Convolution-Based Method [54,55]. In this work, we adopt the mesh-free method with a uniform grid, in which nodes are spaced by a constant distance Δx. Each node represents a portion of the body, called *cell*.

The micro-flux in a bond between the nodes p and q can be computed as

$$\mathrm{j}(\mathbf{x}_p,\mathbf{x}_q,t) = k(\mathbf{x}_p,\mathbf{x}_q,t) \frac{C(\mathbf{x}_q,t) - C(\mathbf{x}_p,t)}{\|\mathbf{x}_q - \mathbf{x}_p\|^2}, \tag{4}$$

where $\mathbf{x}_p$ and $\mathbf{x}_q$ is the position vector of nodes p and q, respectively. The bond property k is either the micro-diffusivity d or the micro-oxidability r (see Remark 2). Therefore, the peridynamic diffusion equation (Eq. (1)) is computed by means of the midpoint quadrature rule in each cell [16–18,49,50]:

$$\frac{\partial C(\mathbf{x}_p,t)}{\partial t} = \sum_{q \in \mathcal{H}_p} \mathrm{j}(\mathbf{x}_p,\mathbf{x}_q,t) \beta_{pq} \Delta x^N, \tag{5}$$

where N is the number of dimensions of the model, so that Δx^N is the length, area or volume of the cell in 1D, 2D or 3D, respectively. As shown in Fig. 6, the index q stands for any node within the neighborhood $\mathcal{H}_p$ of node p and the quadrature coefficient β_{pq} is the fraction of cell of node q lying within $\mathcal{H}_p$.
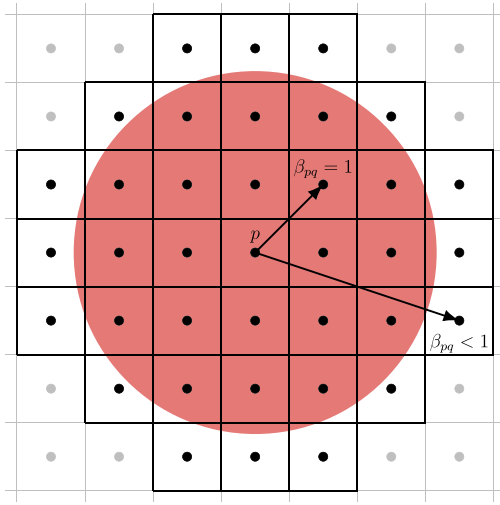
Fig. 6. The neighborhood $\mathcal{H}_p$ (red area) of a node p is constituted by the nodes (black dots) with a portion of their cell within the neighborhood. The quadrature coefficient β_{pq} is the volume fraction of cell of node q lying inside the neighborhood [51]. (For interpretation of the references to color in this figure legend, the reader is referred to the web version of this article.)

Fig. 7. Discretization of a 2D body by means of the meshfree method. The fictitious nodes (empty dots) are added around the body to complete the neighborhoods (red circles) of all the nodes within the body (solid dots). The external surface of the body is discretized using surface nodes (blue solid squares). (For interpretation of the references to color in this figure legend, the reader is referred to the web version of this article.)

Due to the nonlocal nature of the theory, when using the same bond properties determined for points in the bulk for points near the surface, the effective material response is different from the one in the bulk because of incomplete families of points at locations within a horizon size distance away from a material surface. This phenomenon is known as the "peridynamic surface effect" [56]. Examples in which the peridynamics surface effect is desired/useful are when modeling at the atomic scale, or in modeling discrete dislocation dynamics [57,58]. Moreover, peridynamic boundary conditions should be imposed over a finite-thickness layer inside or outside the body [59,60]. However, these issues have been addressed in elastic problems, for example, by means of the surface node method [61–63].

By using this method, we add fictitious nodes around the body, up to a distance δ from the boundary (see Fig. 7). The oxygen concentrations of the fictitious nodes can be determined via the Taylor-based extrapolation truncated at the linear term [61–63]. Moreover, new nodes, namely the *surface nodes*, are introduced at the boundary of the body, as depicted in Fig. 7, and are used to impose the boundary conditions as explained in Appendix A.

3.2. Time integration

For the time integration, the forward Euler method is employed:

$$C(\mathbf{x}_p, t_{n+1}) = C(\mathbf{x}_p, t_n) + \Delta t \, \frac{\partial C(\mathbf{x}_p, t_n)}{\partial t} \,, \qquad (6)$$
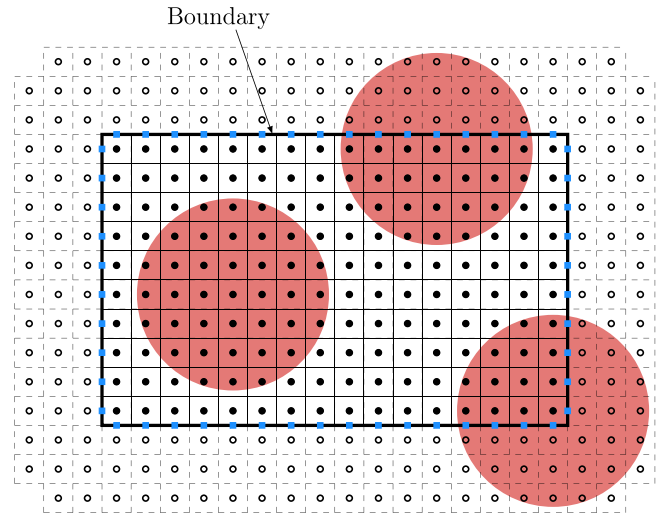
where Δt is the time step size and n is the number of the time step. Therefore, by substituting Eq. (5) into Eq. (6), we obtain:

$$C(\mathbf{x}_p, t_{n+1}) = C(\mathbf{x}_p, t_n) + \Delta t \sum_{q \in \mathcal{H}_p} \mathrm{j}(\mathbf{x}_p, \mathbf{x}_q, t_n) \, \beta_{pq} \, \Delta x^N \,. \qquad (7)$$

For more details about the stability analysis and the convergence studies about the forward Euler method applied to the meshfree method in Peridynamics, see [20].

4. Modeling approach

In this section, we present the methodology employed for modeling the oxidation of ZrC using the PD model framework presented in the previous sections and the underlying rationale. Our approach relies on a thorough examination of the experimental data pertaining to the distribution of oxygen concentration within the layer of material in which the reaction occurs. Subsequently, the peridynamic model for ZrC oxidation is constructed with the aim of reliably predicting the ZrC oxidation mechanism, while employing fewer limiting assumptions in contrast to previous analyses.

The peridynamic model offers several advantages over classical models, including the following:

- Unlike classical models, the peridynamic model does not require the imposition of conditions at the interface, such as the Stefan condition (see, for instance, [18,46–48]). Instead, the motion of the interface is implicitly determined through the "constitutive model" of the material under investigation [18–20].
- Because of the absence of spatial derivatives from the peridynamic formulation, damage is naturally represented, and crack formation can be spontaneous and does not lead to mathematical inconsistencies like they do in PDE-based models. This allows for a more accurate representation of fracture phenomena [64–70].

These advantages collectively contribute to the enhanced capabilities and versatility of the peridynamic model, distinguishing it from classical approaches in the field.

4.1. Analysis of the experimental measurements from [4]

We extract a concentration profile along the depth of the sample using the experimental results obtained in [4] and replotted considering the normalized total oxygen concentration depicted in Fig. 2 (also reproduced in the upper portion of Fig. 8). We chose to consider the region enclosed within the black rectangle in Fig. 2, characterized by the absence of major pores and nearly parallel borders of the intermediate layer. We therefore calculate the average concentrations in the width direction within that region by summing up the oxygen concentrations of all sampled points in the black rectangle in Fig. 8 at the same depth and dividing by the number of those points.

The normalized profile of oxygen concentration is depicted in the lower portion of Fig. 8, revealing the presence of four distinct regions. These regions consist of m-ZrO$_2$ (cracked oxide) spanning from 0 to ~ 9 μm, t-ZrO$_2$ (undamaged oxide) representing the intermediate layer extending from ~ 9 to ~ 12 μm, partially-oxidized ZrC between ~ 12 and ~ 14 μm, and ZrC commencing from ~ 14 μm. The m-ZrO$_2$ region exhibits random oscillations in oxygen concentration, attributable to
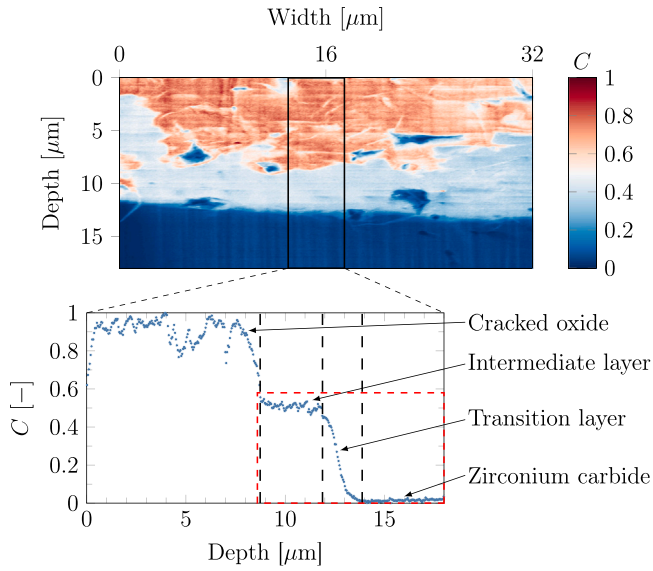
Fig. 8. Normalized oxygen concentration profile (bottom plot) obtained with the average of the experimental data from [4] (SIMS analysis already shown in Fig. 2) along the width of the sample. For the peridynamic model we only consider the portion of the concentration profile contained inside the red dashed rectangle. (For interpretation of the references to color in this figure legend, the reader is referred to the web version of this article.)

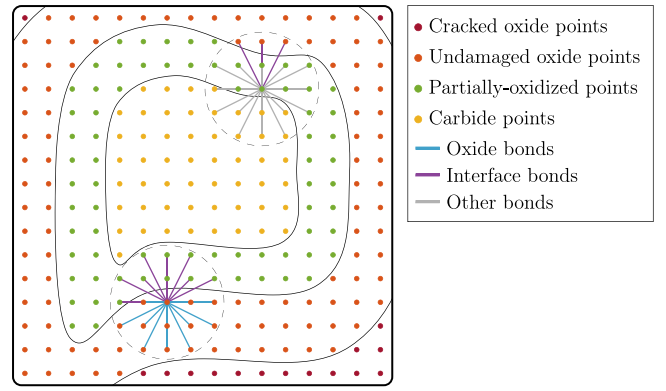**Fig. 9.** Example of possible types of points and bonds.

the presence of cracks. In contrast, the concentration profile within the intermediate layer shows a quasi-linear descent. Meanwhile, the ZrC region is characterized by an oxygen concentration close to zero.

At the interface between m-ZrO$_2$ and t-ZrO$_2$, a sharp jump in concentration, due to oxygen flow within cracks, is observed. However, the interface between t-ZrO$_2$ and ZrC exhibits a gradual transition over a region of thickness ~ 2 μm. Thus, we call this region (where the partially-oxidized phase lies) as "transition layer", as shown in Fig. 8. The transition layer was characterized by Transmission Electron Microscope (TEM) in [71] and is made of amorphous carbon with nanoparticles of ZrC and t-ZrO$_2$ embedded within it. It is worth noting that this transition layer, which acts as the main diffusion barrier, assumes a fundamental role in the overall phenomenon, as will be further discussed subsequently. The layer of cracked oxide is not relevant in the applications we currently consider. Hence, our modeling approach concentrates on capturing solely the effects oxidation has on the region marked by the red rectangle in Fig. 8.

4.2. Modeling of the phase changes

As previously discussed, the region of interest where oxygen diffusion and the oxidation reaction front evolve in time is within the red dashed rectangle in Fig. 8. Therefore, in this section, we describe the modeling approach employed to simulate the diffusion process occurring in the intermediate and transition layers within a peridynamic framework. We disregard, for now, the behavior of the cracked oxide, which can be modeled by the damage mechanism explained in Section 4.3. The ZrC oxidation involves three distinct phases: the oxygen-free zirconium carbide (ZrC), the partially-oxidized phase observed within the transition layer, and the undamaged phase of zirconium oxide (t-ZrO$_2$) present within the intermediate layer. Hence, we name any peridynamic point lying in the carbide phase as "carbide point", in the partially-oxidized phase as "partially-oxidized point", and in the oxide phase as "oxide point".

Since the chemical reaction that transforms the ZrC into ZrO$_2$ is much faster than diffusion, we assume that the phase change between the two is instantaneous in the model. This diffusion-controlled reaction

can be simulated as in the corrosion damage modeling by formulating the nonlocal (peridynamic) version of a simplified Nernst–Planck equation [18], in which the micro-diffusivity (see Eqs. (1) and (2), and Remark 2) becomes:

$$k(\mathbf{x}, \mathbf{x}', t) = \begin{cases} d & \text{if } (\mathbf{x}, \mathbf{x}') \text{ is an oxide bond,} \\ r & \text{if } (\mathbf{x}, \mathbf{x}') \text{ is an interface bond,} \\ 0 & \text{if } (\mathbf{x}, \mathbf{x}') \text{ is any other bond,} \end{cases} \quad (8)$$

where:

- "Oxide bonds" are bonds connecting two (cracked or undamaged) oxide points. The micro-diffusivity d models the diffusion within t-ZrO$_2$ phase and is calibrated to the classical diffusivity D.
- "Interface bonds" are bonds connecting a partially-oxidized point to an oxide point. The micro-oxidability r models the diffusion-controlled reaction between ZrC and t-ZrO$_2$ taking place within the transition layer and is calibrated to the oxidation rate R.
- All the other bonds connecting partially-oxidized or carbide points have zero micro-diffusivity because oxygen diffusion does not occur in those phases.

Fig. 9 illustrates the different types of bonds that are used in the peridynamic model.

To distinguish between oxide and partially-oxidized points, a concentration threshold $\hat{C}_p$ between the two phases is set. A partially-oxidized point transitions into an oxide node when its oxygen concentration is higher than this threshold. The value of the concentration $\hat{C}_p$ can be derived from the experimental data as shown in Section 4.4. This straightforward mechanism enables the modeling of the phase change from ZrC to t-ZrO$_2$ and, simultaneously, governs the motion of the undamaged oxide/ZrC interface.

As the oxygen content of the points within the transition layer starts to rise, a fraction of the zirconium carbide undergoes a transition to the oxidized phase. Since the diffusivity of zirconium oxide is higher than that of the carbide (see Section 5.1) likely due to the volume expansion and the presence of pores/microcracks in the oxide, we suppose that there is an increase in the micro-oxidability as the oxygen content increases. Hence, for simplicity, we consider a linear dependence between the micro-oxidability and the oxygen concentration in regions of partially-oxidized material:

$$r(\mathbf{x}, \mathbf{x}', t) = \left(\bar{r} - \frac{\tilde{r}}{2}\right) + \frac{\tilde{r}}{\hat{C}_p} C(\mathbf{x}_{p\text{-}o}, t), \quad (9)$$

where $C(\mathbf{x}_{p\text{-}o}, t)$ is the oxygen concentration of the partially-oxidized point, $\bar{r}$ is the average of the micro-oxidability of the interface bond, and $\tilde{r}$ is the total variation of the micro-oxidability of the interface bond. Note that interface bonds connect a partially-oxidized point to an oxide point, so the point $\mathbf{x}_{p\text{-}o}$ is the partially-oxidized one between $\mathbf{x}$
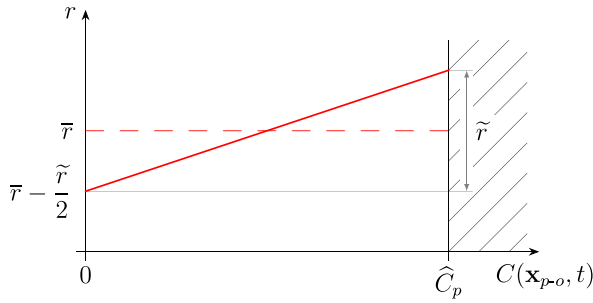
Fig. 10. Micro-oxidability r of an interface bond as a linear function of the concentration $C(\mathbf{x}_{p\text{-}o}, t)$ of the partially-oxidized point. $\bar{r}$ is the average micro-oxidability and $\tilde{r}$ is the total variation of the micro-oxidability for $C(\mathbf{x}_{p\text{-}o}, t)$ varying between 0 and the concentration $\widehat{C}_p$ at which phase change from partially-oxidized to oxide points happens.

Fig. 11. Concentration thresholds derived by the normalized experimental data: $\widehat{C}_m$ is the concentration of the cracked oxide, $\widehat{C}_d$ is the concentration to identify damaged nodes, and $\widehat{C}_p$ is the concentration of phase change. The ~ 2-μm thick transition layer is shown.

and $\mathbf{x}'$. The micro-oxidability as a linear function of the concentration of the partially-oxidized point of the interface bond is shown in Fig. 10. The values $\bar{r}$ and $\tilde{r}$ are empirically obtained with the calibration carried out in Section 5.1.

The values of micro-diffusivity d and micro-oxidability r (i.e., both $\bar{r}$ and $\tilde{r}$) are calibrated via the discretized model presented in Sections 3.1 and 3.2 by comparison with the experimental observations (see Section 5.1). The effects these values have on the oxygen concentration profile are shown in the parametric studies in Appendix B. Note that a constant value of micro-oxidability, i.e., $r = \bar{r} = \text{const.}$ with $\tilde{r} = 0$, does not allow the peridynamic model to accurately reproduce the experimental concentration profile within the transition layer.

4.3. Concentration-driven model for damage evolution

In this work our focus lies on simulating only the effects of the cracked oxide on the intermediate layer. Voids are formed as a result of crack propagation and volumetric expansion within the monoclinic phase of the oxide (m-ZrO$_2$), generating paths for the oxygen to unobstructedly flow towards the external boundary of the intermediate layer. This phenomenon can be effectively represented by a model in which the interface between the cracked and undamaged phases serves as a constant source of oxygen (at constant concentration).

Thus, to determine the extent of damaged oxide, we introduce an additional threshold for oxygen concentration, denoted as $\widehat{C}_d$. When the concentration at a given node overcomes this threshold, the node is defined as damaged. Note that this simplified definition of damage does not include the simulation of crack propagation within the oxide, but, instead, models the effects cracks have on the evolution of the oxidation front. Once a node is classified as damaged, its concentration is set equal to the concentration $\widehat{C}_m$, namely the concentration that the oxide of the intermediate layer "feels" from the cracked oxide. The values of the concentrations $\widehat{C}_d$ and $\widehat{C}_m$ can be obtained from the experimental data as shown in the next section.

4.4. Data extracted from experiments

As shown in Fig. 11, one can determine the appropriate concentration $\widehat{C}_m$ of the damaged oxide, the concentration $\widehat{C}_d$ between the damaged oxide and the intermediate layer, and the oxidation threshold $\widehat{C}_p$. The concentration $\widehat{C}_m$ of the cracked oxide can be established as the maximum concentration shown in Fig. 11. To identify the damaged nodes, the concentration threshold $\widehat{C}_d$ corresponds to the highest concentration within the intermediate layer, i.e., the second-highest concentration in Fig. 11. Regarding the concentration threshold $\widehat{C}_p$ for phase change, it can be selected as an intermediate value between the concentrations at the interface separating t-ZrO$_2$ and ZrC. The values of these concentration thresholds are reported in Fig. 11 and in Table 1. It
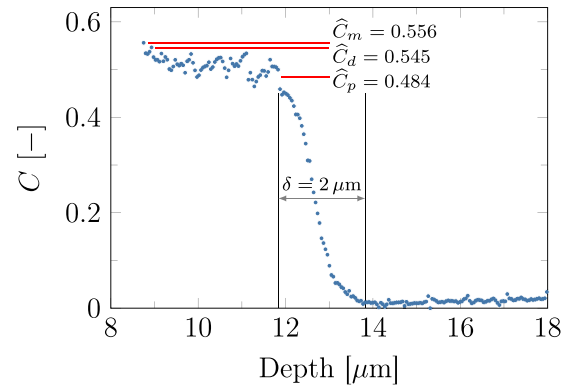
is worth noting that the threshold values are not univocally determined due to measurement uncertainties. However, we carried out several sensitivity studies showing that small deviations from the chosen values change only slightly the results.

Carbide points become partially-oxidized points when their oxygen concentration rises above 0. Since all the bonds connecting carbide or partially oxidized points have zero diffusivity, oxygen can diffuse into a carbide point only through the interface bonds. The maximum length of the interface bonds, as for every bond in the PD model, is equal to the horizon size δ. Therefore, since interface bonds have one end in the oxide phase, the farthest point from the undamaged oxide that can change phase from carbide to partially-oxidized is at a distance equal to δ. This means that, in the PD model, the thickness of the transition layer has to be equal to the horizon size δ. Hence, we select $\delta = 2$ μm, equal to the thickness of the transition layer in the experimental observations (see Fig. 11), in the ZrC oxidation problem.

5. Numerical results for the evolution of the oxidation front in ZrC

In this section, we present the outcomes of the calibration process of the diffusivities, that allows to have good agreement between the experimental data and the 1D peridynamic model. For the first time, the micro-diffusivity of the intermediate layer and the micro-oxidability within the transition layer are accurately calibrated. Additionally, we present results from the 2D model of the same problem and qualitatively compare them with experimental data. For comparable 3D simulations, the present meshfree discretization becomes expensive and either a parallel implementation is required, or the use of the Fast Convolution-Based Method [54,55].

5.1. Calibration of micro-diffusivity and micro-oxidability

The calibration of bond properties is carried out by using the discretization discussed in Sections 3.1 and 3.2 and comparing the 1D numerical results with the experimental observations. In the 1D peridynamic model, a time step size of $\Delta t = 0.01$ s and a grid spacing of $\Delta x = 0.2$ μm are used. As these values are reduced, the accuracy in time and space integration of the peridynamic equations is higher and this may lead to slightly different values of micro-diffusivity and micro-oxidability than those calibrated in this work.

Parametric studies on the values of micro-diffusivity and micro-oxidability are shown in Appendix B. In order to achieve a global concentration distribution similar to the experimental observations, the micro-diffusivity of the oxide is set at $d = 0.5$ μm/s, whereas the average micro-oxidability is $\bar{r} = 0.1$ μm/s (the units of measurements are related to a 1D model, see Eq. (2)). To accurately reproduce the

Table 1

Material parameters and calibrated values for peridynamic quantities for the ZrC oxidation process.

| Property	Value
Maximum concentration	$\widehat{C}_m = 0.556$
Damage concentration	$\widehat{C}_d = 0.545$
Phase change concentration	$\widehat{C}_p = 0.484$
Oxide micro-diffusivity	$d = 0.5 \ \mu m/s$
Average micro-oxidability	$\bar{r} = 0.1 \ \mu m/s$
Variation of micro-oxidability	$\tilde{r} = 0.1 \ \mu m/s$
Oxide diffusivity	$D = 1 \ \mu m^2/s$
Average oxidation rate	$\overline{R} = 0.2 \ \mu m^2/s$
Variation of oxidation rate	$\widetilde{R} = 0.2 \ \mu m^2/s$
Horizon size	$\delta = 2 \ \mu m$
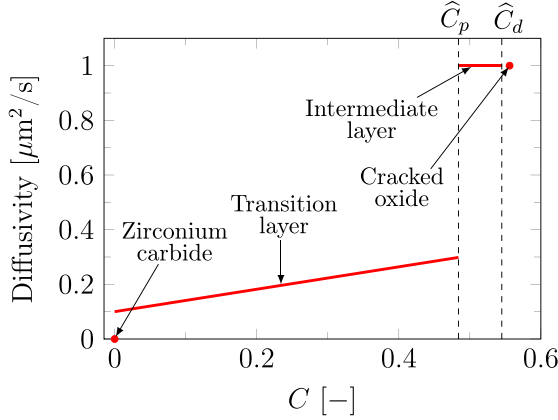
Fig. 12. The diffusion properties (diffusivity or oxidation rate) of the distinct regions of the zirconium carbide during oxidation. The zirconium carbide is characterized by having no oxygen content. The transition layer is characterized by a concentration between 0 and $\widehat{C}_p$ and its oxidation rate increases linearly from $0.1 \ \mu m^2/s$ to $0.3 \ \mu m^2/s$. The intermediate layer (with a concentration comprised between $\widehat{C}_p$ and $\widehat{C}_d$) and the cracked oxide (with a concentration equal to $\widehat{C}_m$) have a diffusivity of $1 \ \mu m^2/s$.

oxygen concentration profile within the transition layer, the variation of the micro-oxidability is chosen as $\tilde{r} = 0.1 \ \mu m^2/s$. This means that the micro-oxidability r varies linearly between $0.05 \ \mu m/s$ and $0.15 \ \mu m/s$ depending on the concentration of the partially-oxidized node.

Table 1 reports the values of micro-diffusivity and micro-oxidability, along with the corresponding values of classical diffusivity (D) and oxidation rate ($\overline{R}$ and $\widetilde{R}$). The classical properties are obtained by multiplying the bond properties by δ (see Eq. (2)). In [4], the oxygen diffusivity was computed as $D = 0.09 \ \mu m^2/s$ following some simplifying assumptions. Dropping those assumptions and using the proposed peridynamic model, the diffusivity is calibrated to be $D = 1 \ \mu m^2 s$. Furthermore, the oxidation rate of the zirconium carbide has been determined for the first time: $R = 0.1 + 0.41 \ C(\mathbf{x}_{p\text{-}o}, t) \ \mu m^2/s$, where $C(\mathbf{x}_{p\text{-}o}, t)$ is the oxygen concentration of the partially-oxidized point. Note that the classical oxidation rate varies linearly as the micro-oxidability, where the average oxidation rate is $\overline{R} = 0.2 \ \mu m^2/s$ and the total variation of the oxidation rate is $\widetilde{R} = 0.2 \ \mu m^2/s$ (see Eq. (9)). The diffusivity/oxidation rate of the distinct regions (depending on the oxygen concentration) is shown in Fig. 12.

Fig. 13 depicts the concentration distribution across the interface, for both the results of the numerical model and the experimental data. The numerical results exhibit a remarkable agreement with the experimental observations. Hence, we can conclude that the chosen values of micro-diffusivity and micro-oxidability employed in the peridynamic model are accurately calibrated.

Remark 3. Fig. 13 is not obtained by data-fitting. The numerical results that are compared with the experimental observations are obtained by means of a peridynamic simulation that, once the material
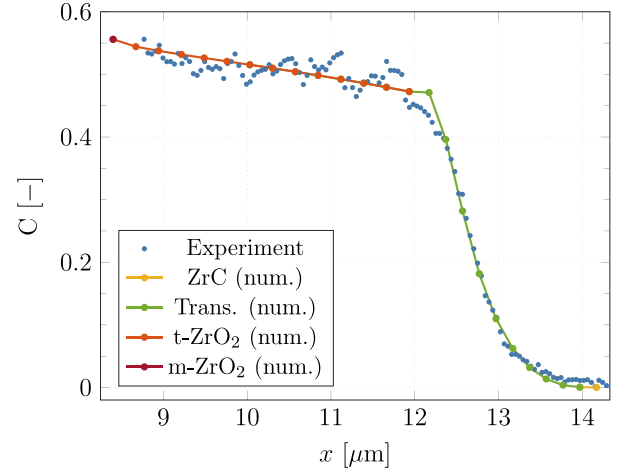
Fig. 13. Experimental data at $1073 \ K$ (blue dots) and numerical results (colored lines) of the concentration profile at $t = 480 \ s$ (see Remark 3). Yellow, green, orange, and red lines represent the numerical results for the zirconium carbide, the transition layer, the intermediate layer, and the cracked oxide, respectively. The numerical results are translated along the x-axis because of Remark 1. (For interpretation of the references to color in this figure legend, the reader is referred to the web version of this article.)

parameters in the model are calibrated to match the thickness of the intermediate layer, predicts the evolution in time of the oxygen concentration profile.

Fig. 14 shows the progressive evolution of the concentration profile at different stages. The initial conditions at $t = 0 \ s$ the node at the boundary has a concentration set to the value of $\widehat{C}_m$ and all the other nodes have no oxygen content. A transient occurs at the beginning of the simulation (see, for example, the plot for $t = 10 \ s$), after which the concentration pattern, in a steady-state condition, gradually advances within the material.

Since the oxide phase is subjected to volume expansion during the phase change, we need to post-process the results in order to estimate the growth of the oxide thickness. Note that the peridynamic approach presented in this paper does not model the volumetric expansion of the oxide phase. This volumetric expansion and the subsequent induced stresses that result in the fragmentation of the oxide will be modeled in future work. By considering a perfect crystal structure, it has been determined that m-ZrO$_2$ exhibits a volume increase of 36% compared to the carbide. Based on this calculations, we estimate in the post-processing stage the thickness of the oxide in the numerical model by increasing the volume of the region occupied by oxide nodes by 36%. Hence, Fig. 15 illustrates that the oxidation interface moves at a constant velocity, in agreement with the experimental results. It is worth keeping in mind that the motion of the interface in a peridynamic diffusion model is not prescribed a priori, but is *predicted* according to the calibrated data in the model.

5.2. Temperature dependence

In this section we analyze how the concentration profile and the speed of the interface vary depending on the temperature. Experiments show that the oxidation process of ZrC at temperatures higher than 1273 K changes significantly and the intermediate layer is no longer present [4]. We therefore use the model to simulate the oxidation behavior at the following additional temperatures: 973 K and 1173 K. Once experimental observations of the concentration profile will be available for temperatures above 1273 K, the proposed model can be modified accordingly.
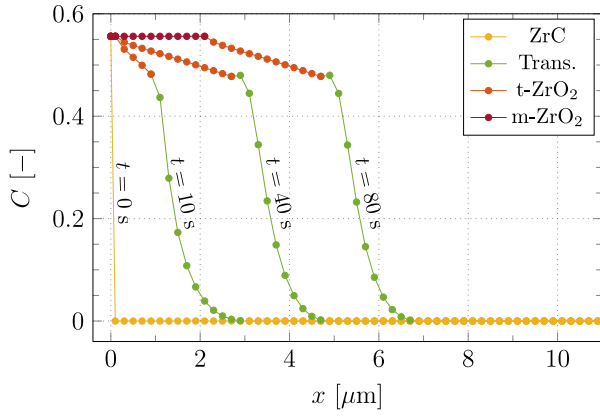
Fig. 14. Normalized oxygen concentration profile at different time instants at a temperature of 1073 K. Yellow, green, orange, and red lines represent the numerical results for the zirconium carbide, the transition layer, the intermediate layer, and the cracked oxide, respectively. (For interpretation of the references to color in this figure legend, the reader is referred to the web version of this article.)
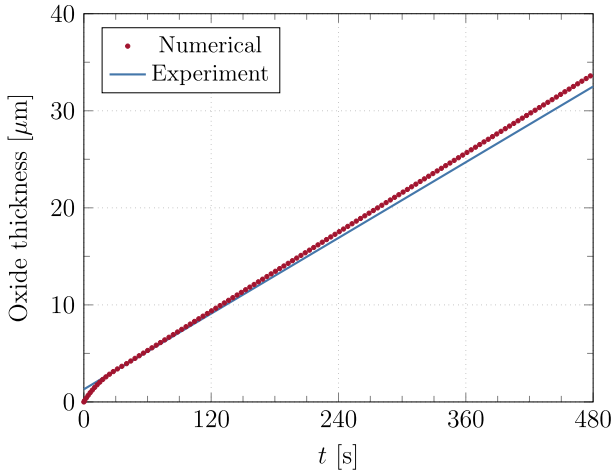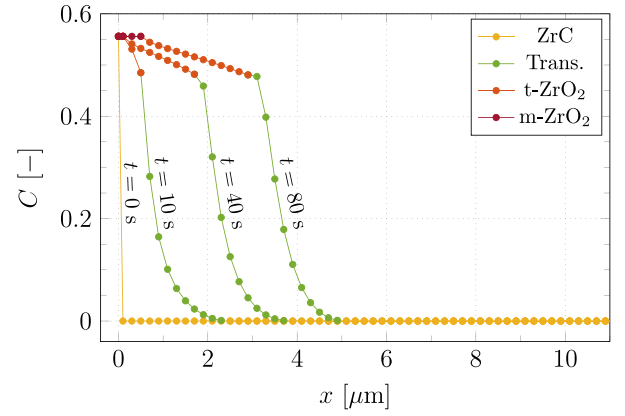

Fig. 16. Normalized oxygen concentration profile at different time instants at a temperature of 973 K. Yellow, green, orange, and red lines represent the numerical results for the zirconium carbide, the transition layer, the intermediate layer, and the cracked oxide, respectively. (For interpretation of the references to color in this figure legend, the reader is referred to the web version of this article.)

Table 2

Propagation speed of the oxidation front for different temperatures obtained from experimental observations in [4] (v_{exp}) and with the proposed model (v_{PD}) based on the calibration data from the experiment at 1073 K.

Temperature	Experiment	Proposed model
$T = 973$ K	–	$v_{PD} = 0.004$ μm/s
$T = 1073$ K	$v_{exp} = 0.065$ μm/s	$v_{PD} = 0.068$ μm/s
$T = 1173$ K	$v_{exp} = 0.069$ μm/s	$v_{PD} = 0.104$ μm/s

Fig. 15. Oxide growth obtained with the proposed model compared to the experimental linear curve-fit. The experimental data has been translated along y-axis because of Remark 1. Note that the slopes of the linear curve-fit and the numerical results, namely the measured and predicted velocities of the interface, are close to each other.

in Eq. (11), respectively, and obtain $D_0 = 160.4$ μm²/s and $R_0 = 505.5$ μm²/s. Therefore, the micro-diffusivity and micro-oxidability (see Eqs. (2), (10), and (11)) are given as $d = 0.297$ μm/s and $\bar{r} = 0.045$ μm/s for $T = 973$ K, and $d = 0.771$ μm/s and $\bar{r} = 0.195$ μm/s for $T = 1173$ K. The linear dependence of the micro-oxidability to the oxygen concentration is assumed to be the same as in Eqs. (9) with $\tilde{r}/\bar{r} = 1$. The same numerical method and discretization parameters described in Section 5.1 are used.

In absence of experimental data for other temperatures, we assume the concentration thresholds ($\widehat{C}_p$, $\widehat{C}_d$, and $\widehat{C}_m$) and transition layer thickness (equal to the horizon size δ), to be the same as those at the 1073 K. This is unlikely to be the case, but here we only attempt to study the trends the model would produce for different temperature conditions.

Figs. 16 and 17 show the concentration profiles for $T = 973$ K and $T = 1173$ K, respectively. Interestingly, the thickness of the intermediate layer slightly increases at higher temperatures. This trend remains to be confirmed in experiments. Furthermore, Table 2 reports the speed of the oxidation front at different temperatures obtained from experimental observations in [4] and with the proposed model. For a temperature of 1173 K, the model gives the correct trend of an increase in interface speed, but because the material data used to calibrate the model parameters were the ones from the 1073 K temperature, the interface moves faster than measured in [4].

5.3. Results from a 2D model

After calibrating the bond properties in the 1D model, we now extend its application to a 2D scenario of oxidation in a square-shape sample. The discretization presented in Sections 3.1 and 3.2 is valid also in 2D. The quadrature coefficients are computed with the algorithm presented in [51]. The PD model of ZrC oxidation can be used both for predicting the growth of the oxide (as in the previous section) and for determining the shape and dimensions of the remaining unoxidized carbide. This section specifically focuses on the latter aspect.

To determine the diffusivity of the zirconium oxide and the oxidation rate of the zirconium carbide at different temperatures, an Arrhenius law is assumed:

$$D = D_0 \exp\left(\frac{\Delta E_{ZrO_2}}{R_g T}\right), \tag{10}$$

$$R = R_0 \exp\left(\frac{\Delta E_{ZrC}}{R_g T}\right), \tag{11}$$

where ΔE_{ZrO_2} and ΔE_{ZrC} are the activation energies for the oxygen diffusion respectively in the oxide and in the carbide, R_g is the universal gas constant, and T is the temperature. The activation energies are reported in literature as $\Delta E_{ZrO_2} = 45.3$ kJmol⁻¹ [72] and $\Delta E_{ZrC} = 69.9$ kJmol⁻¹ [73]. The authors in [72] used the ¹⁸O oxygen gas-solid exchange technique at several temperatures to measure the activation energy of ZrO₂. This approach is similar to that employed in [4], where ¹⁸O was used as a tracer (see Section 2).

To determine the diffusion coefficients D_0 and R_0, we can use the previously calibrated material properties at $T = 1073$ K. In fact, we substitute $T = 1073$ K, $D = 1$ μm²s in Eq. (10) and $R = 0.2$ μm²/s
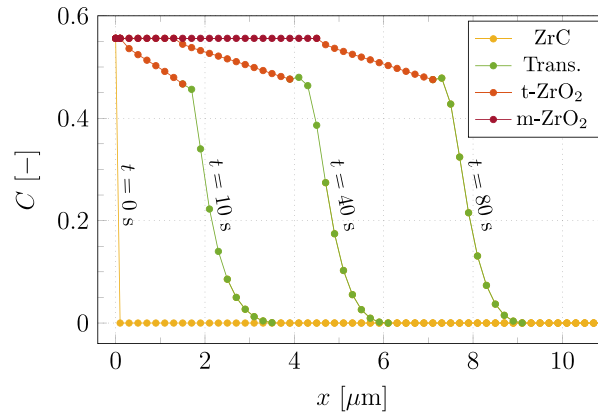
Fig. 17. Normalized oxygen concentration profile at different time instants at a temperature of $1173\,\mathrm{K}$. Yellow, green, orange, and red lines represent the numerical results for the zirconium carbide, the transition layer, the intermediate layer, and the cracked oxide, respectively. (For interpretation of the references to color in this figure legend, the reader is referred to the web version of this article.)
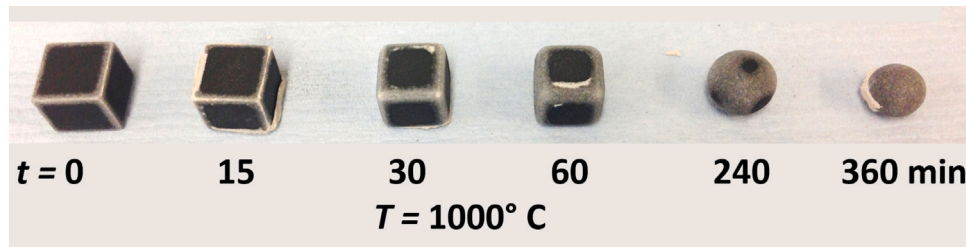

Fig. 18. Shape of the carbide (black material in the bottom portion of the figure) as the oxidation of the sample progresses [74].

As illustrated in Fig. 18 reproduced from [74], the cubic zirconium carbide sample undergoes a transformation under an oxidizing environment, transitioning from its initial cubic shape with sharp corners to a more rounded and eventually spherical shape. This change in morphology occurs due to the accelerated oxidation process at the corners, leading to a faster degradation of material in those regions. Therefore, we expect to obtain the transition from a square to a circular shape of the ZrC in the numerical results of the 2D peridynamic model, in a similar way in which the cube leads to a sphere in the actual experiments (see [74] and Fig. 18).

Peridynamics, due to its nonlocal nature, is known for its high computational cost. Thus, we chose to simulate the oxidation of ZrC in a smaller sample size. As a result, the transition from a square to a circular shape occurs at a faster rate than in the experiment shown in Fig. 18. This also means that our comparison with experimental results will only be qualitative.

The 2D model utilized the same classical material parameters (refer to Table 1) obtained through the calibration process in the 1D scenario. Therefore, using Eq. (2) in the 2D case, the micro-diffusivity is $d \approx 0.32\,\mathrm{s}^{-1}$, the average micro-oxidability is $\bar{r} \approx 0.06\,\mathrm{s}^{-1}$ and the variation of micro-oxidability is $\tilde{r} \approx 0.06\,\mathrm{s}^{-1}$ (the units of measurements are related to a 2D PD model). The computational domain chosen for the 2D simulation is a square with dimensions of $100 \times 100\ \mu\mathrm{m}^2$. A time step size of $\Delta t = 0.01\,\mathrm{s}$ and a grid spacing of $\Delta x = 0.667\ \mu\mathrm{m}$ are used. Similarly to the 1D case, the initial conditions prescribe that the concentrations of the nodes at the boundary are set equal to $\hat{C}_m$, whereas all other nodes have no oxygen content.

Fig. 19 shows the evolution of the concentration field at various time steps during the simulation. The dark blue region represents zirconium carbide with zero oxygen concentration. Initially (see Fig. 19(a)), the carbide shape is a square. As the oxidation front progresses within the material, the corners gradually become rounder (see Figs. 19(b) and 19(c)). In the final stage of the simulation (see Fig. 19(d)), the carbide

shape approximates a circular disk form, which is consistent with the observations from the experimental results in [74]. Furthermore, Fig. 19 shows the amount of cracked oxide (dark red region) predicted by the model at different times, which is higher close to the corners due to the higher surface to volume ratio. Since the surface node method [61–63] with a fictitious layer of nodes is used in the 2D model (see Fig. 7), the horizon, i.e., the nonlocal sphere of influence, is complete also for nodes close to the boundary (and, in particular, to the corners). This means that the PD surface effect plays no role in the faster motion of the interface close to the corners.

With the current discretization, 3D simulations would have a relatively high computational cost, and this is why they are not pursued here. In the future we plan of using special approaches, such as the Fast Convolution-Based Method [54,55], to treat 3D peridynamic models efficiently. The 2D numerical results provided here show good promise for the future 3D model.

6. Conclusions

In this work, we shed light on the evolution of zirconium carbide oxidation process by analyzing the oxygen concentration profile obtained from experimental data and highlighting the presence of two distinct layers across the oxidation front, namely the intermediate and transition layers. We proposed a peridynamic model for oxygen diffusion and oxidation processes that is able to reproduce the oxygen concentration profile and correctly predicts the speed of propagation of the oxidation front measured experimentally. We also analyzed the effects of a temperature variation on the numerical results. Furthermore, the proposed model allows to estimate the growth of the zirconium oxide and determine the shape and dimensions of the remaining zirconium carbide phase. This model can be used for any phenomenon with characteristics similar to the oxidation of zirconium carbide, such as oxidation of transition metal carbides of group IV and lithiation in

(a) $t = 20$ s.

(b) $t = 100$ s.

(c) $t = 240$ s.

(d) $t = 480$ s.
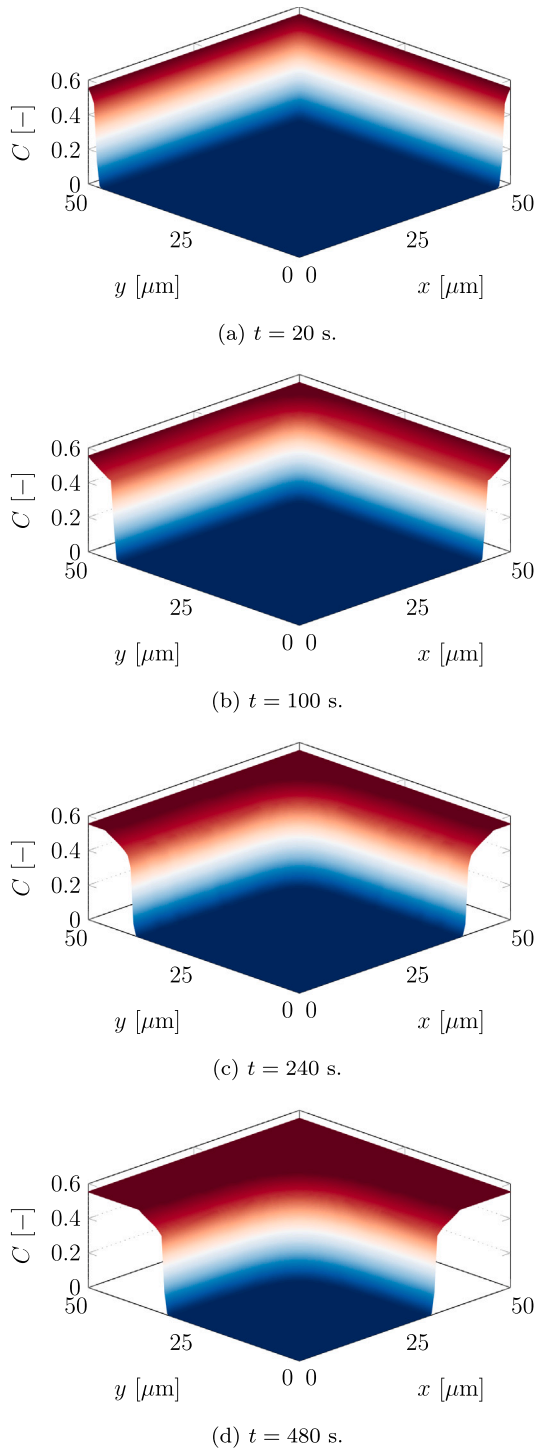
Fig. 19. Normalized oxygen concentration field at different time instants (displayed for one fourth of the square sample thanks to the symmetries of the problem). (For interpretation of the references to color in this figure legend, the reader is referred to the web version of this article.)

solid-state batteries, by recalibrating to the diffusion properties of the specific material system. The model will be further improved in future work by introducing the coupling with the mechanical field to simulate the actual crack/damage initiation and propagation within the oxide. This advancement is expected to enable the model to reproduce the Maltese-cross shape of zirconia and provide a more general framework

for simulating the chemo-mechanical behavior of zirconium carbide and other carbides of interest for energy applications.

CRediT authorship contribution statement

Francesco Scabbia: Writing – original draft, Visualization, Validation, Software, Methodology, Investigation, Formal analysis, Data curation, Conceptualization. **Claudia Gasparrini:** Writing – review & editing, Supervision, Methodology, Investigation, Data curation, Conceptualization. **Mirco Zaccariotto:** Writing – review & editing, Supervision, Methodology, Investigation, Funding acquisition, Conceptualization. **Ugo Galvanetto:** Writing – review & editing, Supervision, Methodology, Investigation, Funding acquisition, Conceptualization. **Florin Bobaru:** Writing – review & editing, Supervision, Resources, Project administration, Methodology, Investigation, Funding acquisition, Formal analysis, Conceptualization.

Declaration of competing interest

The authors declare that they have no known competing financial interests or personal relationships that could have appeared to influence the work reported in this paper.

Acknowledgments

Funded by the European Union
NextGenerationEU

Appendix A. Imposition of peridynamic boundary conditions via the surface node method

To impose the peridynamic boundary conditions, we adopt the surface node method [63]. A new type of nodes, i.e., the *surface nodes*, are introduced to discretize the boundary of the body, as depicted in Fig. 7: in 1D, 2D and 3D each surface node represents respectively a boundary point, a segment of length Δx and a square with area Δx^2. A surface node $\mathbf{x}_s$ with normal $\mathbf{n}_s$ is governed by the following equation based on the concept of peridynamic flux [63]:

$$J(\mathbf{x}_s, \mathbf{n}_s, t) = - \sum_{pq \in \mathcal{I}} \alpha_{pq} \, \mathrm{j}(\mathbf{x}_p, \mathbf{x}_q, t) \left(\mathbf{m}_{pq} \cdot \mathbf{n}_s \right) \beta_{pq} \, \Delta x^{N+1} \,, \tag{A.1}$$

where J is the external flux, $\mathcal{I}$ is the set of all the bonds, $\mathbf{m}_{pq}$ is the bond direction unit vector, and N is the number of dimensions of the model. α_{pq} is a coefficient given as follows (see [62,63] for more details and figures):

- In 1D, 2D or 3D, $\alpha_{pq} = 0$ if the bond does not intersect the boundary region associated to the surface node s.
- In 3D, $\alpha_{pq} = 1/4$ if the bond intersects the corner of the square associated to the surface node s (the bond is "shared" among four surface nodes) or $\alpha_{pq} = 1/2$ if the bond intersects the edge of the square (the bond is "shared" between two surface nodes).
- In 2D, $\alpha_{pq} = 1/2$ if the bond intersects the end of the segment associated to the surface node s (the bond is "shared" between two surface nodes).
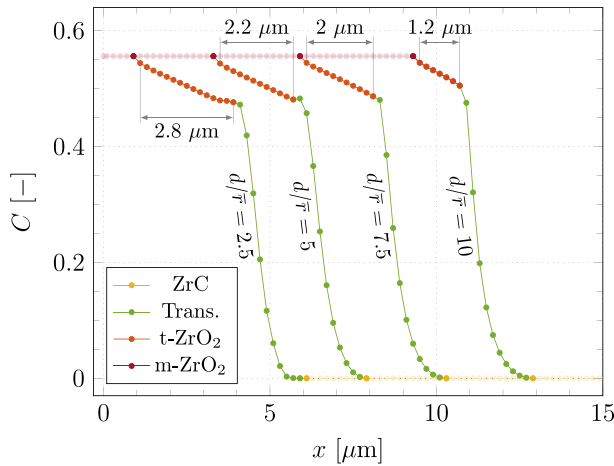
Fig. B.1. Normalized oxygen concentration across the oxidation interface at $t = 100\,\text{s}$ for different ratios between the micro-diffusivity d of the oxide phase and the average micro-oxidability $\bar{r}$. The plots are obtained by using a value of average micro-oxidability equal to $\bar{r} = 0.1\,\mu\text{m/s}$.

Table B.1
Propagation speed of the oxidation front for different values of diffusivity. The following values are obtained by using an average micro-oxidability equal to $\bar{r} = 0.1$ μm/s.

| Diffusivity ratio	Oxidation front speed
$d/\bar{r} = 2.5$	$v_{PD} = 0.05$ μm/s
$d/\bar{r} = 5$	$v_{PD} = 0.068$ μm/s
$d/\bar{r} = 7.5$	$v_{PD} = 0.096$ μm/s
$d/\bar{r} = 10$	$v_{PD} = 0.127$ μm/s

- $\alpha_{pq} = 1$ otherwise.

The boundary conditions can be imposed directly on the surface nodes as one would do in a local model [63]: a concentration $\overline{C}(t)$ at a surface node s is imposed as $C(\mathbf{x}_s, t) = \overline{C}(t)$ and a flux $\overline{J}(t)$ through the surface node s is imposed as $J(\mathbf{x}_s, \mathbf{n}_s, t) = \overline{J}(t)$.

Appendix B. Parametric studies

The modeling approach using the peridynamic framework described in Section 4 is based on the calibration of the values of micro-diffusivity d of the oxide phase and the micro-oxidability r. The micro-oxidability is modeled as a linear function of the oxygen concentration of the partially-oxidized node, and is univocally determined by the values of the average micro-oxidability $\bar{r}$ and the micro-oxidability variation $\tilde{r}$ (see Eq. (9)). In this section, we perform two parametric studies to show how the "shape" of the concentration profile across the oxidation interface changes depending on the ratios $d/\bar{r}$ and $\tilde{r}/\bar{r}$.

The numerical results of the normalized oxygen concentration for different values of the ratio $d/\bar{r}$ are shown in Fig. B.1. It is evident that, by increasing $d/\bar{r}$, the propagation speed of the oxidation front is higher and the thickness of the intermediate layer is reduced (see Table B.1). Differences in oxygen concentration profiles within the transition layer are negligible. These results are used in Section 5.1 for the calibration of the ratio $d/\bar{r}$ in order to obtain in the numerical model a thickness of the intermediate layer similar to the one observed in the experiments. In the model of ZrC oxidation, the chosen value of $d/\bar{r}$ is 5 so that we match the thickness of the intermediate layer measured in the experiments in [4] at 1073 K (see Fig. 13).

The value of the ratio $\tilde{r}/\bar{r}$ affects the normalized oxygen concentration profile only within the transition layer, as shown in Fig. B.2. For higher values of the ratio $\tilde{r}/\bar{r}$, the slope of the concentration distribution in the transition layer increases accordingly. Therefore,
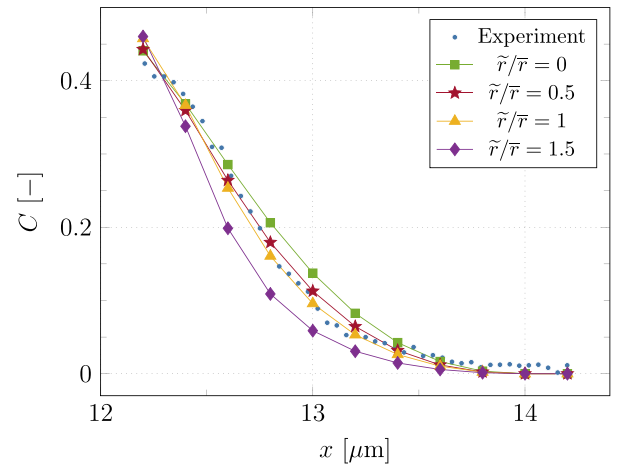
Fig. B.2. Normalized oxygen concentration within the transition layer at $t = 100\,\text{s}$ for different ratios between the micro-oxidability variation $\tilde{r}$ and the average micro-oxidability $\bar{r}$. The plots are obtained by using a value of average micro-oxidability equal to $\bar{r} = 0.1$ μm/s. The numerical results are translated along the x-axis because of Remark 1.

the value of $\tilde{r}/\bar{r} = 1$ is chosen in Section 5.1 so that we match the slope of the concentration profile of the transition layer observed in the experimental measurements in [4] at 1073 K (see Fig. 13).

Data availability

Data will be made available on request.

References

[1] S. Maloy, K. Natesan, D. Holcomb, C. Fazio, P. Yvon, Overview of reactor systems and operational environments for structural materials in Gen-IV fission reactors, in: Structural Alloys for Nuclear Energy Applications, Elsevier, 2019, pp. 23–49, http://dx.doi.org/10.1016/B978-0-12-397046-6.00002-2.

[2] K. Verfondern, H. Nabielek, J. Kendall, Coated particle fuel for high temperature gas cooled reactors, Nucl. Eng. Technol. 39 (5) (2007) 603, http://dx.doi.org/10.5516/NET.2007.39.5.603.

[3] Y. Katoh, G. Vasudevamurthy, T. Nozawa, L. Snead, Properties of zirconium carbide for nuclear fuel applications, J. Nucl. Mater. 441 (1–3) (2013) 718–742, http://dx.doi.org/10.1016/j.jnucmat.2013.05.037.

[4] C. Gasparrini, R. Chater, D. Horlait, L. Vandeperre, W. Lee, Zirconium carbide oxidation: Kinetics and oxygen diffusion through the intermediate layer, J. Am. Ceram. Soc. 101 (6) (2018) 2638–2652, http://dx.doi.org/10.1111/jace.15479.

[5] C. Gasparrini, D. Rana, N. Le Brun, D. Horlait, C. Markides, I. Farnan, W. Lee, On the stoichiometry of zirconium carbide, Sci. Rep. 10 (1) (2020) 6347, http://dx.doi.org/10.1038/s41598-020-63037-0.

[6] T. Davey, Y. Chen, The effect of oxygen impurities on the stability and structural properties of vacancy-ordered and -disordered ZrCx, RSC Adv. 12 (6) (2022) 3198–3215, http://dx.doi.org/10.1039/D1RA07768F.

[7] S. Maharjan, X. Zhang, Z. Wang, Effect of oxide growth strain in residual stresses for the deflection test of single surface oxidation of alloys, Oxid. Met. 77 (2012) 93–106, http://dx.doi.org/10.1007/s11085-011-9275-1.

[8] A. Aryanfar, A. El Tallis, J. Marian, Coupling the corrosion-and pressure-assisted stress buildup within the zirconium in PWR pipes, JOM 75 (1) (2023) 120–131, http://dx.doi.org/10.1007/s11837-022-05503-w.

[9] C. Gasparrini, R. Podor, D. Horlait, M. Rushton, O. Fiquet, W. Lee, Oxidation of UC: an in situ high temperature environmental scanning electron microscopy study, J. Nucl. Mater. 494 (2017) 127–137, http://dx.doi.org/10.1016/j.jnucmat.2017.07.016.

[10] C. Gasparrini, R. Podor, O. Fiquet, D. Horlait, S. May, M. Wenman, W. Lee, Uranium carbide oxidation from 873 K to 1173 K, Corros. Sci. 151 (2019) 44–56, http://dx.doi.org/10.1016/j.corsci.2019.01.044.

[11] A. Paul, J. Binner, B. Vaidhyanathan, UHTC composites for hypersonic applications, in: Ultra-High Temperature Ceramics: Materials for Extreme Environment Applications, Wiley Online Library, 2014, pp. 144–166, http://dx.doi.org/10.1002/9781118700853.ch7.

[12] P. Platt, P. Frankel, M. Gass, R. Howells, M. Preuss, Finite element analysis of the tetragonal to monoclinic phase transformation during oxidation of zirconium alloys, J. Nucl. Mater. 454 (1–3) (2014) 290–297, http://dx.doi.org/10.1016/j.jnucmat.2014.08.020.

[13] M. Pettinà, R. Harrison, L. Vandeperre, F. Biglari, P. Brown, W. Lee, K. Nikbin, Diffusion-based and creep continuum damage modelling of crack formation during high temperature oxidation of ZrN ceramics, J. Eur. Ceram. Soc. 36 (9) (2016) 2341–2349, http://dx.doi.org/10.1016/j.jeurceramsoc.2015.11.023.

[14] S. Silling, Reformulation of elasticity theory for discontinuities and long-range forces, J. Mech. Phys. Solids 48 (1) (2000) 175–209, http://dx.doi.org/10.1016/S0022-5096(99)00029-0.

[15] S. Silling, M. Epton, O. Weckner, J. Xu, E. Askari, Peridynamic states and constitutive modeling, J. Elasticity 88 (2) (2007) 151–184, http://dx.doi.org/10.1007/s10659-007-9125-1.

[16] F. Bobaru, M. Duangpanya, The peridynamic formulation for transient heat conduction, Int. J. Heat Mass Transfer 53 (19–20) (2010) 4047–4059, http://dx.doi.org/10.1016/j.ijheatmasstransfer.2010.05.024.

[17] F. Bobaru, M. Duangpanya, A peridynamic formulation for transient heat conduction in bodies with evolving discontinuities, J. Comput. Phys. 231 (7) (2012) 2764–2785, http://dx.doi.org/10.1016/j.jcp.2011.12.017.

[18] Z. Chen, F. Bobaru, Peridynamic modeling of pitting corrosion damage, J. Mech. Phys. Solids 78 (2015) 352–381, http://dx.doi.org/10.1016/j.jmps.2015.02.015.

[19] S. Jafarzadeh, Z. Chen, F. Bobaru, Peridynamic modeling of repassivation in pitting corrosion of stainless steel, Corrosion 74 (4) (2018) 393–414, http://dx.doi.org/10.5006/2615.

[20] F. Scabbia, C. Gasparrini, M. Zaccariotto, U. Galvanetto, A. Larios, F. Bobaru, Moving interfaces in peridynamic diffusion models and influence of discontinuous initial conditions: Numerical stability and convergence, Comput. Math. Appl. 151 (2023) 384–396, http://dx.doi.org/10.1016/j.camwa.2023.10.016.

[21] A. Vasenkov, Multi-physics peridynamic modeling of damage processes in protective coatings, J. Peridyn. Nonlocal Model. 3 (2) (2021) 167–183, http://dx.doi.org/10.1007/s42102-020-00046-7.

[22] D. Behera, P. Roy, E. Madenci, S. Oterkus, Prediction of thermal oxidation damage in polymers by using peridynamics, in: 2021 IEEE 71st Electronic Components and Technology Conference, ECTC, IEEE, 2021, pp. 1457–1463, http://dx.doi.org/10.1109/ECTC32696.2021.00232.

[23] P. Platt, R. Mella, W. DeMaio, M. Preuss, M. Wenman, Peridynamic simulations of the tetragonal to monoclinic phase transformation in zirconium dioxide, Comput. Mater. Sci. 140 (2017) 322–333, http://dx.doi.org/10.1016/j.commatsci.2017.09.001.

[24] T. Haynes, A. Battistini, A. Leide, D. Liu, L. Jones, D. Shepherd, M. Wenman, Peridynamic modelling of cracking in TRISO particles for high temperature reactors, J. Nucl. Mater. (2023) 154283, http://dx.doi.org/10.1016/j.jnucmat.2023.154283.

[25] M. McDowell, S. Lee, W. Nix, Y. Cui, 25Th anniversary article: Understanding the lithiation of silicon and other alloying anodes for lithium-ion batteries, Adv. Mater. 25 (36) (2013) 4966–4985, http://dx.doi.org/10.1002/adma.201301795.

[26] V. Deshpande, R. McMeeking, Models for the interplay of mechanics, electrochemistry, thermodynamics, and kinetics in lithium-ion batteries, Appl. Mech. Rev. 75 (1) (2023) 010801, http://dx.doi.org/10.1115/1.4056289.

[27] M. Pharr, K. Zhao, X. Wang, Z. Suo, J. Vlassak, Kinetics of initial lithiation of crystalline silicon electrodes of lithium-ion batteries, Nano Lett. 12 (9) (2012) 5039–5047, http://dx.doi.org/10.1021/nl302841y.

[28] M. Pharr, Z. Suo, J. Vlassak, Measurements of the fracture energy of lithiated silicon electrodes of Li-ion batteries, Nano Lett. 13 (11) (2013) 5570–5577, http://dx.doi.org/10.1021/nl403197m.

[29] S. Huang, F. Fan, J. Li, S. Zhang, T. Zhu, Stress generation during lithiation of high-capacity electrode particles in lithium ion batteries, Acta Mater. 61 (12) (2013) 4354–4364, http://dx.doi.org/10.1016/j.actamat.2013.04.007.

[30] Z. Ma, T. Li, Y. Huang, J. Liu, Y. Zhou, D. Xue, Critical silicon-anode size for averting lithiation-induced mechanical failure of lithium-ion batteries, RSC Adv. 3 (20) (2013) 7398–7402, http://dx.doi.org/10.1039/C3RA41052H.

[31] C. Becker, K. Strawhecker, Q. McAllister, C. Lundgren, In situ atomic force microscopy of lithiation and delithiation of silicon nanostructures for lithium ion batteries, ACS Nano 7 (10) (2013) 9173–9182, http://dx.doi.org/10.1021/nn4037909.

[32] H. Cho, M. Glazer, Q. Xu, H. Han, D. Dunand, Numerical and experimental investigation of (de)lithiation-induced strains in bicontinuous silicon-coated nickel inverse opal anodes, Acta Mater. 107 (2016) 289–297, http://dx.doi.org/10.1016/j.actamat.2016.01.064.

[33] F. Shi, Z. Song, P. Ross, G. Somorjai, R. Ritchie, K. Komvopoulos, Failure mechanisms of single-crystal silicon electrodes in lithium-ion batteries, Nature Commun. 7 (1) (2016) 11886, http://dx.doi.org/10.1038/ncomms11886.

[34] S. Zhang, Chemomechanical modeling of lithiation-induced failure in high-volume-change electrode materials for lithium ion batteries, NPJ Comput. Mater. 3 (1) (2017) 7, http://dx.doi.org/10.1038/s41524-017-0009-z.

[35] S. Basu, N. Koratkar, Y. Shi, Structural transformation and embrittlement during lithiation and delithiation cycles in an amorphous silicon electrode, Acta Mater. 175 (2019) 11–20, http://dx.doi.org/10.1016/j.actamat.2019.05.055.

[36] Z. Zhang, N. Liao, H. Zhou, W. Xue, Insight into silicon-carbon multilayer films as anode materials for lithium-ion batteries: A combined experimental and first principles study, Acta Mater. 178 (2019) 173–178, http://dx.doi.org/10.1016/j.actamat.2019.08.009.

[37] Z. Chen, G. Zhang, F. Bobaru, The influence of passive film damage on pitting corrosion, J. Electrochem. Soc. 163 (2) (2015) C19, http://dx.doi.org/10.1149/2.0521602jes.

[38] S. Jafarzadeh, Z. Chen, F. Bobaru, Computational modeling of pitting corrosion, Corros. Rev. 37 (5) (2019) 419–439, http://dx.doi.org/10.1515/corrrev-2019-0049.

[39] S. Jafarzadeh, Z. Chen, J. Zhao, F. Bobaru, Pitting, lacy covers, and pit merger in stainless steel: 3D peridynamic models, Corros. Sci. 150 (2019) 17–31, http://dx.doi.org/10.1016/j.corsci.2019.01.006.

[40] S. Jafarzadeh, Z. Chen, S. Li, F. Bobaru, A peridynamic mechano-chemical damage model for stress-assisted corrosion, Electrochim. Acta 323 (2019) 134795, http://dx.doi.org/10.1016/j.electacta.2019.134795.

[41] Z. Chen, S. Jafarzadeh, J. Zhao, F. Bobaru, A coupled mechano-chemical peridynamic model for pit-to-crack transition in stress-corrosion cracking, J. Mech. Phys. Solids 146 (2021) 104203, http://dx.doi.org/10.1016/j.jmps.2020.104203.

[42] J. Zhao, S. Jafarzadeh, M. Rahmani, Z. Chen, Y. Kim, F. Bobaru, A peridynamic model for galvanic corrosion and fracture, Electrochim. Acta 391 (2021) 138968, http://dx.doi.org/10.1016/j.electacta.2021.138968.

[43] S. Jafarzadeh, J. Zhao, M. Shakouri, F. Bobaru, A peridynamic model for crevice corrosion damage, Electrochim. Acta 401 (2022) 139512, http://dx.doi.org/10.1016/j.electacta.2021.139512.

[44] F. Bobaru, M. Yang, L. Alves, S. Silling, E. Askari, J. Xu, Convergence, adaptive refinement, and scaling in 1D peridynamics, Internat. J. Numer. Methods Engrg. 77 (6) (2009) 852–877, http://dx.doi.org/10.1002/nme.2439.

[45] Z. Chen, F. Bobaru, Selecting the kernel in a peridynamic formulation: A study for transient heat diffusion, Comput. Phys. Comm. 197 (2015) 51–60, http://dx.doi.org/10.1016/j.cpc.2015.08.006.

[46] A. Visintin, Introduction to stefan-type problems, in: Handbook of Differential Equations: Evolutionary Equations, vol. 4, Elsevier, 2008, pp. 377–484, http://dx.doi.org/10.1016/S1874-5717(08)00008-X.

[47] S. Mitchell, M. Vynnycky, On the numerical solution of two-phase Stefan problems with heat-flux boundary conditions, J. Comput. Appl. Math. 264 (2014) 49–64, http://dx.doi.org/10.1016/j.cam.2014.01.003.

[48] M. Khalid, M. Zubair, M. Ali, An analytical method for the solution of two phase Stefan problem in cylindrical geometry, Appl. Math. Comput. 342 (2019) 295–308, http://dx.doi.org/10.1016/j.amc.2017.09.013.

[49] S. Silling, E. Askari, A meshfree method based on the peridynamic model of solid mechanics, Comput. Struct. 83 (17–18) (2005) 1526–1535, http://dx.doi.org/10.1016/j.compstruc.2004.11.026.

[50] P. Seleson, Improved one-point quadrature algorithms for two-dimensional peridynamic models based on analytical calculations, Comput. Methods Appl. Mech. Engrg. 282 (2014) 184–217, http://dx.doi.org/10.1016/j.cma.2014.06.016.

[51] F. Scabbia, M. Zaccariotto, U. Galvanetto, Accurate computation of partial volumes in 3D peridynamics, Eng. Comput. 39 (1) (2023) 959–991, http://dx.doi.org/10.1007/s00366-022-01725-3.

[52] Q. Du, L. Tian, X. Zhao, A convergent adaptive finite element algorithm for nonlocal diffusion and peridynamic models, SIAM J. Numer. Anal. 51 (2) (2013) 1211–1234, http://dx.doi.org/10.1137/120871638.

[53] Q. Du, L. Ju, L. Tian, K. Zhou, A posteriori error analysis of finite element method for linear nonlocal diffusion and peridynamic models, Math. Comp. 82 (284) (2013) 1889–1922, http://dx.doi.org/10.1090/S0025-5718-2013-02708-1.

[54] S. Jafarzadeh, A. Larios, F. Bobaru, Efficient solutions for nonlocal diffusion problems via boundary-adapted spectral methods, J. Peridyn. Nonlocal Model. 2 (1) (2020) 85–110, http://dx.doi.org/10.1007/s42102-019-00026-6.

[55] S. Jafarzadeh, L. Wang, A. Larios, F. Bobaru, A fast convolution-based method for peridynamic transient diffusion in arbitrary domains, Comput. Methods Appl. Mech. Engrg. 375 (2021) 113633, http://dx.doi.org/10.1016/j.cma.2020.113633.

[56] Q. Le, F. Bobaru, Surface corrections for peridynamic models in elasticity and fracture, Comput. Mech. 61 (4) (2018) 499–518, http://dx.doi.org/10.1007/s00466-017-1469-1.

[57] W. Dong, H. Liu, J. Du, X. Zhang, M. Huang, Z. Li, Z. Chen, F. Bobaru, A peridynamic approach to solving general discrete dislocation dynamics problems in plasticity and fracture: Part I. Model description and verification, Int. J. Plast. 157 (2022) 103401, http://dx.doi.org/10.1016/j.ijplas.2022.103401.

[58] W. Dong, H. Liu, J. Du, X. Zhang, M. Huang, Z. Li, Z. Chen, F. Bobaru, A peridynamic approach to solving general discrete dislocation dynamics problems in plasticity and fracture: Part II. Applications, Int. J. Plast. 159 (2022) 103462, http://dx.doi.org/10.1016/j.ijplas.2022.103462.

[59] E. Madenci, E. Oterkus, Peridynamic Theory and Its Applications, vol. 17, Springer, 2014, http://dx.doi.org/10.1007/978-1-4614-8465-3.

[60] F. Bobaru, J. Foster, P. Geubelle, S. Silling, Handbook of Peridynamic Modeling, CRC Press, 2016, books.google.it/books?id=cBgNDgAAQBAJ.

[61] F. Scabbia, M. Zaccariotto, U. Galvanetto, A novel and effective way to impose boundary conditions and to mitigate the surface effect in state-based peridynamics, Internat. J. Numer. Methods Engrg. 122 (20) (2021) 5773–5811, http://dx.doi.org/10.1002/nme.6773.

[62] F. Scabbia, M. Zaccariotto, U. Galvanetto, A new method based on Taylor expansion and nearest-node strategy to impose Dirichlet and Neumann boundary conditions in ordinary state-based Peridynamics, Comput. Mech. 70 (1) (2022) 1–27, http://dx.doi.org/10.1007/s00466-022-02153-2.

[63] F. Scabbia, M. Zaccariotto, U. Galvanetto, A new surface node method to accurately model the mechanical behavior of the boundary in 3D state-based peridynamics, J. Peridyn. Nonlocal Model. (2023) 1–35, http://dx.doi.org/10.1007/s42102-022-00094-1.

[64] P. Qiao, M. Yang, F. Bobaru, Impact mechanics and high-energy absorbing materials, J. Aerosp. Eng. 21 (4) (2008) 235–248, http://dx.doi.org/10.1061/(ASCE)0893-1321(2008)21:4(235).

[65] F. Bobaru, Y. Ha, W. Hu, Damage progression from impact in layered glass modeled with peridynamics, Cent. Eur. J. Eng. 2 (2012) 551–561, http://dx.doi.org/10.2478/s13531-012-0020-6.

[66] W. Hu, Y. Wang, J. Yu, C. Yen, F. Bobaru, Impact damage on a thin glass plate with a thin polycarbonate backing, Int. J. Impact Eng. 62 (2013) 152–165, http://dx.doi.org/10.1016/j.ijimpeng.2013.07.001.

[67] M. Zaccariotto, F. Luongo, U. Galvanetto, G. Sarego, Examples of applications of the peridynamic theory to the solution of static equilibrium problems, Aeronaut. J. 119 (1216) (2015) 677–700, http://dx.doi.org/10.1017/S0001924000010770.

[68] F. Bobaru, G. Zhang, Why do cracks branch? A peridynamic investigation of dynamic brittle fracture, Int. J. Fract. 196 (1–2) (2015) 59–98, http://dx.doi.org/10.1007/s10704-015-0056-8.

[69] G. Zhang, G. Gazonas, F. Bobaru, Supershear damage propagation and sub-Rayleigh crack growth from edge-on impact: A peridynamic analysis, Int. J. Impact Eng. 113 (2018) 73–87, http://dx.doi.org/10.1016/j.ijimpeng.2017.11.010.

[70] Z. Xu, G. Zhang, Z. Chen, F. Bobaru, Elastic vortices and thermally-driven cracks in brittle materials with peridynamics, Int. J. Fract. 209 (2018) 203–222, http://dx.doi.org/10.1007/s10704-017-0256-5.

[71] C. Gasparrini, R. Podor, D. Horlait, R. Chater, W. Lee, Zirconium carbide oxidation: Maltese cross formation and interface characterization, Oxid. Met. 88 (2017) 509–519, http://dx.doi.org/10.1007/s11085-016-9672-6.

[72] F. Keneshea, D. Douglass, The diffusion of oxygen in zirconia as a function of oxygen pressure, Oxid. Met. 3 (1) (1971) 1–14, http://dx.doi.org/10.1007/BF00604736.

[73] A. Kuriakose, J. Margrave, The oxidation kinetics of zirconium diboride and zirconium carbide at high temperatures, J. Electrochem. Soc. 111 (7) (1964) 827, http://dx.doi.org/10.1149/1.2426263.

[74] C. Gasparrini, Oxidation of Zirconium and Uranium Carbides (Ph.D. thesis), Imperial College London, 2018, http://dx.doi.org/10.25560/59006.